Proc. Natl. Acad. Sci. USA
Vol. 94, pp. 4848–4852, May 1997
Mathematics

A fast, high resolution, second-order central scheme for incompressible flows

(hyperbolic conservation laws/second-order accuracy/central difference schemes/nonoscillatory schemes)

RAZ KUPFERMAN* AND EITAN TADMOR†‡

*Mathematics Department, Lawrence Berkeley National Laboratory, 1 Cyclotron Road, 50A–2152, Berkeley, CA 94720; †School of Mathematical Sciences, Tel-Aviv University, Tel-Aviv 69978 Israel; and ‡Department of Mathematics, University of California, Los Angeles, CA 90095

Communicated by Alexandre J. Chorin, University of California, Berkeley, CA, March 10, 1997 (received for review December 1, 1996)

ABSTRACT **A high resolution, second-order central difference method for incompressible flows is presented. The method is based on a recent second-order extension of the classic Lax–Friedrichs scheme introduced for hyperbolic conservation laws (Nessyahu H. & Tadmor E. (1990) *J. Comp. Physics.* 87, 408-463; Jiang G.-S. & Tadmor E. (1996) UCLA CAM Report 96-36, *SIAM J. Sci. Comput.*, in press) and augmented by a new discrete Hodge projection. The projection is exact, yet the discrete Laplacian operator retains a compact stencil. The scheme is fast, easy to implement, and readily generalizable. Its performance was tested on the standard periodic double shear-layer problem; no spurious vorticity patterns appear when the flow is underresolved. A short discussion of numerical boundary conditions is also given, along with a numerical example.**

The accurate computation of flow problems is of major importance in many fields of science and engineering. Many of the modern high resolution methods used for such computations use the Godunov approach, in which the time evolution of a piecewise polynomial approximation of the flow field is sought. Typically, this piecewise polynomial approximate solution is reconstructed from its cell averages. In this context, we distinguish between two main classes of methods: upwind and central methods.

Upwind schemes evaluate cell averages at the center of the piecewise polynomial elements, which in turn requires the evaluation of fluxes along the cell interfaces. Consequently, upwind schemes must take into account the characteristic speeds along such interfaces. Special attention is required at those interfaces in which there is a combination of forward- and backward-going waves, when it is necessary to decompose the "Riemann fan" and determine the separate contribution of each component by tracing "the direction of the wind." It is the need to trace characteristic fans (using exact or approximate Riemann solvers) that greatly complicates the upwind algorithms, making them difficult to implement and to generalize to more complex systems (e.g., to viscoelastic fluids). The original first order accurate Godunov scheme (1) is the forerunner for all other upwind Godunov-type schemes. A variety of second and higher order sequels to the Godunov upwind scheme was constructed, analyzed, and implemented with great success during the 1970s and 1980s, starting with van Leer's monotonic upstream scheme for conservation laws (2) (followed by ref. 3–6; see refs. 7–9 and the references therein). For incompressible flows, the upwind Godunov approach was combined with Chorin's projection technique (10) by Bell, Colella, and Glaz (11), E and Shu (12), and others (consult ref. 13 and the references therein).

In this work, we used the central differences framework. In contrast to upwind schemes, central schemes evaluate staggered cell averages at the breakpoints between the piecewise polynomial elements. Thus, averages are integrated over the entire Riemann fan so that the corresponding fluxes are now evaluated at the smooth centers of the cells. Consequently, costly Riemann-solvers required in the upwind framework can be now replaced by straightforward quadrature rules. The first order Lax–Friedrichs (LxF) scheme (14) is the canonical example of such central difference schemes. Like Godunov's scheme, the central LxF scheme is based on a piecewise constant approximate solution. Its Riemann-solver-free recipe, however, is considerably simpler. Unfortunately, the LxF scheme introduces excessive numerical viscosity, resulting in relatively poor resolution.

Nessyahu and Tadmor (15) introduced a second order sequel to the central LxF scheme in one spatial dimension. Like its second order, upwind MUSCL analogue, the Nessyahu–Tadmor scheme is based on a piecewise–linear polynomial approximation, which yields a considerable improvement in resolution; at the same time, the central averaging results in a simple Riemann-solver-free recipe. The Nessyahu–Tadmor scheme recently was extended to higher orders (16) and several spatial dimensions (17). Numerical experiments reported above and in related work (18–20) show that the central schemes offer a considerably simpler alternative to the upwind schemes while retaining a comparable resolution.

The central schemes mentioned above were introduced primarily for hyperbolic systems of conservation laws, such as those governing compressible flows. These encouraging results motivated the use of central differences in related problems, notably for incompressible flows. The two-dimensional Euler equation in its vorticity formulation was addressed along these lines in Levy and Tadmor (21). It is the goal of this paper to introduce a second-order central difference scheme for incompressible flows based on velocity variables. The use of the velocity formulation (1) yields a more versatile algorithm. The advantage of our proposed central scheme in its velocity formulation is 2-fold: Generalization to the three-dimensional case is straightforward, and the treatment of boundary conditions associated with general geometries becomes simpler. The result is a simple, fast, high resolution method, whose accuracy is comparable to that of an upwind scheme. In addition, numerical experiments show the new scheme to be immune to some of the well known deleterious consequences of underresolution.

THE SECOND-ORDER CENTRAL SCHEME

We considered a two-dimensional incompressible flow field, $\mathbf{u} = (u, v)$, so that $\nabla\cdot\mathbf{u} = 0$. The equations of motion for a Newtonian fluid in conservation form are

The publication costs of this article were defrayed in part by page charge payment. This article must therefore be hereby marked "*advertisement*" in accordance with 18 U.S.C. §1734 solely to indicate this fact.

0027-8424/97/944848-5$2.00/0
PNAS is available online at **http://www.pnas.org**.

Abbreviations: BM, Brown and Minion; LxF, Lax–Friedrichs.

$$u_t = [-u^2 + \nu u_x - p]_x + [-uv + \nu u_y]_y$$
$$\equiv f^u(u, v, u_x, \dots)_x + g^u(u, v, u_x, \dots)_y$$
$$v_t = [-uv + \nu v_x]_x + [-v^2 + \nu v_y - p]_y$$
$$\equiv f^v(u, v, u_x, \dots)_x + g^v(u, v, u_x, \dots)_y \quad [1]$$

where p is the pressure, ν is the kinematic viscosity, and subscripts denote partial derivatives. The functions $f^{u,v}(\cdot)$ and $g^{u,v}(\cdot)$ are components of the fluxes of the conserved quantities u and v.

We now turn to the derivation of our central scheme. The computational grid consists of rectangular cells of sizes Δx and Δy; at time level $t^n = n\Delta t$, these cells, $C_{i,j}$, are centered at $(x_i = i\Delta x, y_j = j\Delta y)$. Starting with the corresponding cell averages, $\mathbf{u}^n = (u^n_{i,j}, v^n_{i,j})$, we first reconstructed a piecewise linear polynomial approximation that recovers the point values of the velocity field $\mathbf{u}^n(x, y) = (u^n(x, y), v^n(x, y))$. For second-order accuracy, the piecewise–linear reconstructed velocities take the form,

$$\mathbf{u}^n(x, y) = \mathbf{u}^n_{i,j} + \frac{\mathbf{u}'_{i,j}}{\Delta x}(x - x_i) + \frac{\mathbf{u}_{i,j}}{\Delta y}(y - y_j), x, y \in C_{i,j}. \quad [2]$$

Here and below, $\mathbf{u}'_{i,j}/\Delta x$ and $\mathbf{u}_{i,j}/\Delta y$ are discrete slopes in the x and y directions, which are reconstructed from the given cell averages. To guarantee second-order accuracy, these slopes should approximate the corresponding x and y derivatives of the underlying solution. To avoid spurious oscillations, the recipe for construction of such slopes requires certain nonlinear limiters—a variety of such recipes was studied extensively during the 1980s (see refs. 2, 22, and 23 and the references therein). In the numerical examples reported below, however, we found that the evaluation of the slopes $\mathbf{u}'$, $\mathbf{u}$, using simple centered differences without limiters sufficed.

The second stage was to evolve the piecewise–linear approximant to the next time level t^{n+1}. The resulting solution, $\tilde{\mathbf{u}}^{n+1}(x, y) = (\tilde{u}^{n+1}(x, y), \tilde{v}^{n+1}(x, y))$, is projected back into the space of piecewise constant polynomials. We denote this piecewise constant solution by $\tilde{\mathbf{u}}$. It is a nonzero divergence field, and it is therefore considered a provisional field (this requires a third and final stage of the evolution step, in which we compute its zero divergence projection, $\mathbf{u}^{n+1}$). Specifically, we realized $\tilde{\mathbf{u}}^{n+1}(x, y)$ by its staggered cell averages $\tilde{\mathbf{u}}^{n+1}_{i+1/2,j+1/2} := \fint_{C_{i+1/2,\,j+1/2}} \tilde{\mathbf{u}}^{n+1}(x, y)dxdy$. (Throughout this paper, we use $\fint_\Omega := 1/|\Omega| \int_\Omega$ to denote normalized integrals, scaled by their length, area, volume, etc.). The central differencing feature of our scheme is linked to staggered cells, $C_{i+1/2,\,j+1/2}$ centered around $(x_{i+1/2}, y_{j+1/2})$. To evaluate these staggered averages, we integrate Eq. 1 over the control box $C_{i+1/2,\,j+1/2} \times [t^n, t^{n+1}]$. Consider now the difference between the cell averages at the top and at the bottom of this box; in view of the conservation form of Eq. 1, this difference is balanced solely by the flux across the box's interfaces (see Fig. 1),

$$\tilde{u}_{i+1/2,j+1/2}(t^{n+1}) = \fint_{C_{i+1/2,j+1/2}} u(x, y, t^n)dxdy$$
$$+ \Delta t\{D^+_x \fint_{\tau=t^n}^{t^{n+1}} \fint_{y\in J_{j+1/2}} f^u(x_i, y, \tau)dyd\tau\}$$
$$+ \Delta t\{D^+_y \fint_{\tau=t^n}^{t^{n+1}} \fint_{x\in I_{i+1/2}} g^u(x, y_j, \tau)dxd\tau\}. \quad [3]$$

A similar averaging applies for $\tilde{v}^{n+1}_{i+1/2,j+1/2}$. Here and below, $D^+_x w_i = (w_{i+1,.} - w_{i,.})/\Delta x$ and $\mu^+_x w_{i,.} = 1/2(w_{i+1,.} + w_{i,.})$ denote, respectively, forward differences and forward averages in the x direction. The meaning of the related operators such as D^+_y, D^-_x, $\mu^\pm_y$, ... is self-evident; in particular, $\nabla^2_h = D^+_x D^-_x + D^+_y D^-_y$ is the standard 5-point Laplacian.

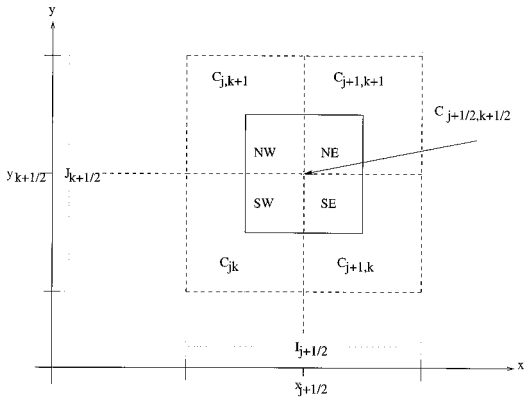

FIG. 1. The staggered grid.

We now turn to the (approximate) evaluation of the terms on the right-hand side of Eq. 3. The staggered cell average at the bottom on the box, $\fint_{C_{i+1/2,j+1/2}} u(x, y, t^n)dxdy$, involves contributions from the four intersecting cells, $C_{i,j}$, $C_{i+1,j}$, $C_{i+1,j+1}$, and $C_{i,j+1}$ indicated in Fig. 1. A straightforward computation yields

$$\fint_{C_{i+1/2,j+1/2}} u(x, y, t^n)dxdy = \mu^+_x \mu^+_y u^n_{i,j}$$
$$- \frac{\Delta x}{8} D^+_x \mu^+_y u'_{i,j} - \frac{\Delta y}{8} D^+_y \mu^+_x u_{i,j}. \quad [4]$$

It remains to integrate the fluxes f^u, g^u, ... across the interfaces of the control box. For second-order accuracy, the double integrals on the right of Eq. 3 are approximated by suitable averages of their corner values. Thus, for example, a combination of the second-order trapezoidal and mid-point quadrature rules yields the following approximation for the flux associated with $f^u = -u^2 + \nu u_x - p_x$,

$$D^+_x \fint_{\tau=t^n}^{t^{n+1}} \fint_{y\in J_{j+1/2}} f^u(x_i, y, \tau)dyd\tau$$
$$\sim D^+_x \left[-\mu^+_y (u^{n+1/2}_{i,j})^2 + \frac{\nu}{2}\left(\mu^+_y \frac{u'_{i,j}}{\Delta x} + D^-_x \tilde{u}^{n+1}_{i+1/2,j+1/2} \right) \right]. \quad [5]$$

Similar approximations are used for the remaining fluxes associated with f^v, g^u, g^v. Few remarks are in order, clarifying the motivation for this type of central discretization:

- Two of the four relevant fluxes appearing in Eq. 1, f^u and g^v, involve the pressure gradient (p_x, p_y), which could be viewed as a Lagrange multiplier enforcing the zero divergence constraint, $\nabla\cdot\mathbf{u} = 0$. Our approximation of these two fluxes, e.g., Eq. 5, ignores the pressure gradient at this stage. Here, we follow the projection method (10, 11), which separates the time evolution from the incompressibility constraint by first evolving the flow field without taking pressure into account. The contribution of the pressure will be integrated at the last stage by enforcing zero divergence fluxes.
- Temporal integration of the viscosity terms $\nu u_x, \dots$ is accomplished by second-order averaging at t^n and t^{n+1}. This quadrature leads to the implicit Crank–Nicholson discretization, which is favored because of its preferable stability properties.
- The temporal integration of the convective part of the flux, however (represented by the quadratic terms like u^2, $uv, \dots$), is accomplished by the midpoint rule evaluated at $t^{n+1/2}$. This requires the intermediate values $u^{n+1/2}_{i,j}$ and

$v^{n+1/2}_{i,j}$. It is here that we take advantage of the central framework; because the cell centers (x_i, y_j) are bounded away from the discontinuous breakpoints, we may use Taylor expansion to compute these midvalues. Thus, the first ingredient of our scheme consists of the following.

Predictor step.

$$u^{n+1/2}_{i,j} = u^n_{i,j} - \frac{\Delta t}{2}\Big[2u^n_{i,j}\frac{u'_{i,j}}{\Delta x} + u^n_{i,j}\frac{v'_{i,j}}{\Delta y} + v^n_{i,j}\frac{u'_{i,j}}{\Delta y} + G_x p^n_{i,j} - \nu\nabla^2_h u_{i,j}\Big]$$

$$v^{n+1/2}_{i,j} = v^n_{i,j} - \frac{\Delta t}{2}\Big[v^n_{i,j}\frac{u'_{i,j}}{\Delta x} + u^n_{i,j}\frac{v'_{i,j}}{\Delta x} + 2v^n_{i,j}\frac{u'_{i,j}}{\Delta y} + G_y p^n_{i,j} - \nu\nabla^2_h u_{i,j}\Big] \quad [6]$$

Note that the predictor step is nothing but a forward Euler scheme; conservation form is not essential for the spatial discretization at this stage.

Equipped with the midvalues of $\mathbf{u}^{n+1/2}_{i,j} := (u^{n+1/2}_{i,j}, v^{n+1/2}_{i,j})$, we can now compute the approximate fluxes in Eq. 5; these together with Eq. 4 yield the staggered averages at t^{n+1}, which we summarize in the following section.

Corrector step.

$$\Big(1 - \frac{\nu\Delta t}{2}\nabla^2_h\Big)\tilde{\mathbf{u}}^{n+1}_{i+1/2,j+1/2} = \mu^+_x\mu^+_y\mathbf{u}^n_{i,j} - \frac{\Delta x}{8}D^+_x\mu^+_y\mathbf{u}'_{i,j} - \frac{\Delta y}{8}D^+_y\mu^+_x\mathbf{u}'_{i,j} - \Delta t D^+_x\mu^+_y\Big[u^{n+1/2}_{i,j}\mathbf{u}^{n+1/2}_{i,j} - \frac{\nu\mathbf{u}'_{i,j}}{2\Delta x}\Big] - \Delta t D^+_y\mu^+_x\Big[v^{n+1/2}_{i,j}\mathbf{u}^{n+1/2}_{i,j} - \frac{\nu\mathbf{u}'_{i,j}}{2\Delta y}\Big]. \quad [7]$$

The corrector step, Eq. 7 evaluates a nondivergence-free provisional field, $\tilde{\mathbf{u}}^{n+1}$. At the third and final stage of the computation, we have to evaluate the zero divergence projection of this provisional field. This zero divergence constraint in turns determines the pressure gradient. We note that satisfying an appropriate, discrete zero divergence constraint is intrinsically related to the finite speed of propagation of the velocity field $\mathbf{u}$, and consequently, it is essential for the stability of the scheme. Indeed, the zero divergence constraint enables us to rewrite the scheme (Eq. 7) in an appropriate convective form, which in turns yields a maximum upper bound. Such a program was carried out by Levy and Tadmor (21); in their study, a maximum principle was derived based on a convective reformulation of the vorticity equation. Granted the finite speed of propagation of the velocity field $\mathbf{u}$, one may revisit the predictor step with the usual Courant–Friedrichs–Levy time step limitation $\max\{\Delta t/\Delta x|u|, \Delta t/\Delta y|v|\} \le 1/2$. We note in passing that hyperbolicity is not necessary for the stability of the central NT scheme (15, 17); finite speed of propagation will suffice.

We now turn to the computation of the incompressible projection. We decomposed the provisional field $\tilde{\mathbf{u}}^{n+1}$ into the sum of a divergence-free flow field, $\mathbf{u}^{n+1} := (u^{n+1}, v^{n+1})$, and a gradient field of a scalar grid function, $\phi_{i,j}$ (11),

$$\tilde{u}^{n+1}_{i+1/2,j+1/2} = u^{n+1}_{i+1/2,j+1/2} + \Delta t D^+_x\mu^+_y\phi_{i,j},$$

$$\tilde{v}^{n+1}_{i+1/2,j+1/2} = v^{n+1}_{i+1/2,j+1/2} + \Delta t D^+_y\mu^+_x\phi_{i,j},$$

where the new field $\mathbf{u}^{n+1}_{i+1/2,j+1/2} = (u^{n+1}_{i+1/2,j+1/2}, v^{n+1}_{i+1/2,j+1/2})$ has to satisfy the zero divergence condition,

$$D^-_x\mu^-_y u^{n+1}_{i+1/2,j+1/2} + D^-_y\mu^-_x v^{n+1}_{i+1/2,j+1/2} = 0. \quad [8]$$

This dictates the scalar potential $\phi_{i,j}$, which is calculated by solving the corresponding Poisson problem. Thus, we end up with the following step.

Projection step. Compute the potential $\phi_{i,j}$ solving the Poisson equation

$$[D^+_xD^-_x\mu^+_y\mu^-_y + D^+_yD^-_y\mu^+_x\mu^-_x]\phi_{i,j} = \frac{1}{\Delta t}[D^-_x\mu^-_y\tilde{u}^{n+1}_{i+1/2,j+1/2} + D^-_y\mu^-_x\tilde{v}^{n+1}_{i+1/2,j+1/2}]. \quad [9]$$

Then, the pressure gradient at t^{n+1} is being updated,

$$G_x p^{n+1}_{i+1/2,j+1/2} := D^+_x\mu^+_y\phi_{i,j},\ \ G_y p^{n+1}_{i+1/2,j+1/2} := D^+_y\mu^+_x\phi_{i,j}, \quad [10]$$

and finally, it is used to evaluate the divergence-free velocity field, $\mathbf{u}^{n+1}$

$$\mathbf{u}^{n+1}_{i+1/2,j+1/2} = \tilde{\mathbf{u}}^{n+1}_{i+1/2,j+1/2} - \Delta t\mathbf{G}_x p^{n+1}_{i+1/2,j+1/2}. \quad [11]$$

It is noteworthy that our projection operator P is exact, i.e., $P^2 = P$, and it is substantially simpler in comparison with the original Bell, Colella, and Glaz projection (11). Thus, for example, the Poisson equation (Eq. 9) becomes a particularly simple 5-point star stencil (for a square grid, $\Delta x = \Delta y$).

Numerical Experiments. We turn now to numerical examples that demonstrate the efficiency of our proposed central scheme (Eqs. 6–7, 9–11). All of our computations were carried out with the Courant–Friedrichs–Levy limitation $\max\{\Delta t/\Delta x|u|, \Delta t/\Delta y|v|\} = 0.45$.

The first example is a double shear layer governed by the Navier–Stokes equations (Eq. 1), in a unit 1-periodic domain, subject to the initial conditions

$$u^\rho_0(x,y) = \begin{cases}\tanh[\rho(y-1/4)] & y \le 1/2\\ \tanh[\rho(3/4-y)] & y > 1/2,\end{cases}$$

$$v^\delta_0(x,y) = \delta\sin(2\pi x). \quad [12]$$

The parameter ρ determines the slope of the shear layer, and v^δ_0 represents a small perturbation of the steady solution, (u^ρ_0, v^0_0). The initial layer rolls up in time into strong vortical structures. This problem is a canonical test problem for a scheme's accuracy and resolution in incompressible flows. Brown and Minion (BM) (13) performed for this problem a systematic comparison between a number of schemes, concentrating on the effect of underresolution. Their results will serve as a reference.

Underresolution and stability. In Fig. 2, we plot vorticity contours for the two shear layer problems discussed by BM (13): the inviscid "thick" shear layer problem corresponding to (u^ρ_0, v^δ_0) with $\rho = 30$ and a viscous "thin" shear layer problem (with $\nu = 5{\cdot}10^{-5}$), corresponding to (u^ρ_0, v^δ_0) with $\rho = 100$. As in BM (13), both plots in Fig. 2 are recorded at time $t = 1.2$ and are subject to an initial perturbation v^δ_0, with $\delta = 0.05$.

The vorticity contour plot for the thick shear layer (Fig. 2*a*) is comparable to the corresponding upwind results reported by BM (13). For the thin layer, however, the results of the central scheme are qualitatively different. When the upwind solution of the thin shear layer problem was underresolved, BM (13) observed the formation of spurious vortices, as additional roll-ups develop; these additional vortices are found with both upwind and spectral methods and eventually cause the calculation to break down. (The spurious nature of these vortices is confirmed only as the mesh is further refined and these vortices disappear). In contrast, the effect of underresolution on our scheme is an increased numerical viscosity that smears the vorticity distribution. Yet the central scheme has the advan-

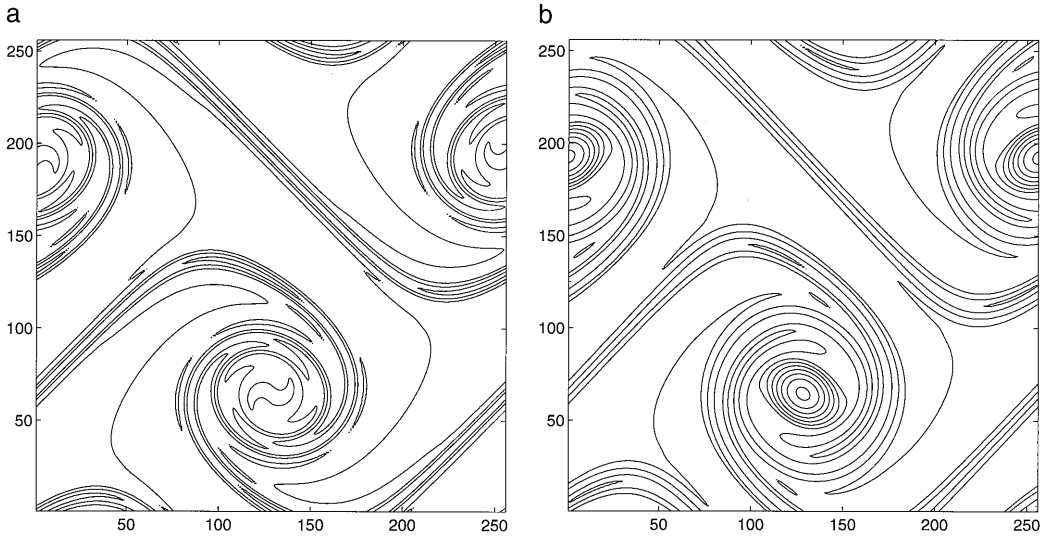

FIG. 2. Contour lines of the vorticity $\omega = v_x - u_y$ at $t = 1.2$ with initial (u^ρ, v^δ), $\delta = 0.05$ using a 256×256 grid. (*a*) A thick shear layer with $\rho = 30$ and $\nu = 0$. The contour levels range from -36 to 36 (*cf.* figure 3*c* in ref. 13). (*b*) A thin shear layer with $\rho = 100$ and $\nu = 5{\cdot}10^{-5}$. The contour levels range from -70 to 70 (*cf.* figure 9*b* in ref. 13).

tage that it does not introduce new unphysical vorticity patterns. No spurious pattern was observed as the resolution was further decreased down to a 32×32 grid. Thus, the stability of our central method appears to prevent the formation of any underresolution-induced structure although the method is less accurate than an upwind scheme for a given grid. The issues of accuracy, resolution, and stability as inspected in Fig. 2 may, of course, vary with different parameterizations. We carried out additional (unreported) numerical experiments, measuring vorticity contours and enstrophy behavior with varying νs and Ns. These experiments reconfirmed the high resolution content of our central scheme, resolution comparable to the upwind results; at the same time, they showed that our central scheme was immuned to spurious oscillations because of underresolution. We note that this demonstrates again that accuracy and resolution may be two distinct qualities of a scheme (24).

Efficiency. The central scheme has improved stability properties that prevent spurious vortices due to underresolution. What is the cost of regaining this stability in comparison to the upwind schemes? Table 1 presents L^2 errors for our calculation of the inviscid double shear layer problem subject to initial data (u_0^ρ, v_0^δ) with $\rho = 30$. Here, u_N represents the numerical approximation computed at time $t = 1.2$ using $N \times N$ spatial grid points.

The convergence rate was estimated by Richardson extrapolation. The asymptotic convergence rate is approached only as the resolution becomes sufficiently high so that there are enough points to resolve the shear layer. Compared to the results in BM, our errors are about three to four times larger. Thus, to obtain similar errors, our scheme would roughly require a grid twice as dense. For a given grid size, however, our scheme results in a code up to five times faster than a parallel upwind scheme. Therefore, it is $\approx$60% more time-consuming for a given accuracy.

Boundary conditions. The treatment of nontrivial boundary conditions requires special attention because the numerical grid is translated by one-half of a grid cell at each time step while the physical boundaries remain fixed in space. For example, if an edge cell lies entirely inside the system after a given time step, only half of it will lie inside the system after the next step. In most respects, the treatment of the boundaries fits naturally into the recipe given above; only slight changes are required. In particular, numerical derivatives at walls have to be evaluated by one-sided expressions. The boundary conditions on the projection operator are more delicate. The following treatment results in second-order convergence: When the centers of the edge cells lie on the boundary, the prescribed boundary values, $\mathbf{u}_{bc}$, are explicitly imposed, that is, $\mathbf{G_x}\phi = \tilde{\mathbf{u}} - \mathbf{u}_{bc}$. In the remaining cases, it is the incompressibility condition (Eq. 8) that is imposed.

As an example, we present the results for flow in a two-dimensional channel with immobile parallel walls. Periodic boundary conditions are assumed for the longitudinal axis. Fig. 3 shows a succession of flow profiles $u(y)$ for a realization in which the initial conditions are a uniform longitudinal flow. At time $t = 0$, infinite shear gradients are formed and then

Table 1. L_2 error and extrapolated convergence rates for the double shear layer problem (Eq. 12) with $\rho = 30$, $\delta = 0.05$, and $\nu = 0$ at $t = 1.2$

	$n = 32$	$n = 64$	$n = 128$
$\|u_N - u_{2N}\|_{L^2}$	0.143	0.0627	0.0172
Rate	1.19	1.86	

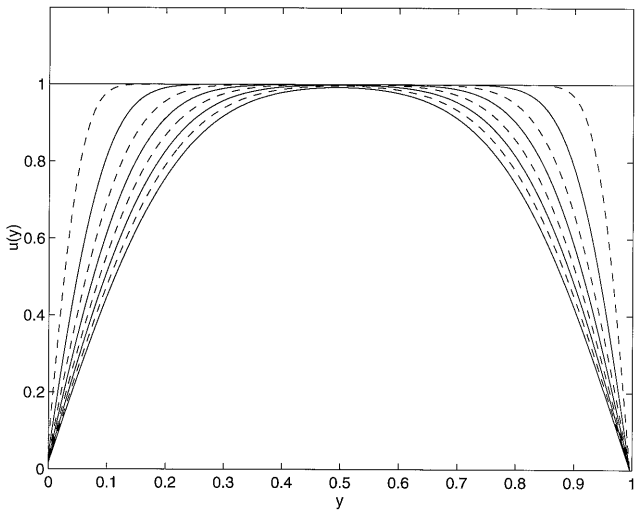

FIG. 3. A viscous flow (with $\nu = 0.01$) in a channel with immobile walls subject to initial conditions $u_0(x, y) \equiv 1$, $v_0(x, y) \equiv 0$. Number of grid points is 128×128. The successive solid and dashed lines represent the flow profiles $u(y)$ at times $t = 0, .1, .3, .5, \ldots, 1.5$.

gradually smoothed out by the viscous forces. Note the resolution at the shear walls. In this context, it is worth repeating that no limiters (2, 22, 23) were used.

CONCLUSIONS

We have presented a numerical scheme for incompressible flows that offers significant improvement over available methods in terms of simplicity, adaptability, and resolution, with only a small loss of accuracy per given amount of labor. In two respects, the performance of our scheme is particularly noteworthy: Low resolution and sharp gradients do not result in spurious structures, and limiters are unnecessary. These observations are consistent with previous results using the staggered central scheme in the context of hyperbolic conservation laws (15–17), in particular the results of Levy and Tadmor (21), regarding the robustness of the staggered central scheme; it is not clear whether the two manifestations of robustness mentioned above are due to the same reason. We have observed this robustness of staggered centered schemes in other contexts and shall report on it in more detail elsewhere.

The authors are grateful to Profs. A. Chorin and A. Majda for suggesting the combination of central schemes with the projection method and to Prof. A. Chorin for a critical reading of the manuscript. R.K. also benefited from useful conversations with Profs. P. Colella, M. Denn, and D. Gottlieb and Dr. A. Kast and from the assistance of Dr. D. Adalsteinsson on programming issues. This work was supported by the U.S. Department of Energy under contract DE-AC03-76SF-00098, by U.S. National Science Foundation Grant DMS94-04942, and by U.S. Office of Naval Research contract N00014-91-J-1076.

1. Godunov, S. K. (1959) *Mat. Sbomik.* **47,** 271–306.
2. van Leer, B. (1979) *J. Comp. Physics* **32,** 101–136.
3. Roe, P. (1981) *J. Comp. Physics* **43,** 357–372.
4. Harten, A. (1983) *J. Comp. Physics* **49,** 357–393.
5. Osher, S. (1984) *SIAM J. Numer. Anal.* **21,** 217–235.
6. Colella, P. & Woodward, P. (1984) *J. Comp. Physics* **54,** 174–201.
7. Godlewski, E. & Raviart, P.-A. (1996) *Numerical Approximation of Hyperbolic Systems of Conservation Laws* (Springer, New York).
8. LeVeque, R. J. (1992) *Numerical Methods for Conservation Laws* (Birkhaeuser, Boston).
9. Hirsch, C. (1988) *Numerical Computation of Internal and External Flows* (Wiley, New York).
10. Chorin, A. J. (1969) *Math. Comp.* **22,** 745–762.
11. Bell, J. B., Colella, P. & Glaz, H. M. (1989) *J. Comp. Physics* **85,** 257–283.
12. E., W. & Shu, C.-W. (1993) *J. Comp. Physics* **110,** 39–46.
13. Brown, D. L. & Minion, M. L. (1995) *J. Comp. Physics* **122,** 165–183.
14. Lax, P. D. (1954) *Commun. Pure Appl. Math.* **7,** 159–193.
15. Nessyahu, H. & Tadmor, E. (1990) *J. Comp. Physics* **87,** 408–463.
16. Liu. X.-D. & Tadmor, E. (1997) *Numer. Math*., in press.
17. Jiang, G. S. & Tadmor, E. (1996) *SIAM J. Sci. Comput*., in press.
18. Sanders, R. & Weiser, A. (1992) *J. Comp. Physics* **101,** 314–329.
19. Huynh, H. T. (1995) Proceedings of the 12th American Institute of Aeronautics and Astronautics (AIAA) Conference (AIAA, San Diego).
20. Tadmor, E. & Wu, C. C. *Central Scheme for the Multidimensional MHD Equations*, Submitted.
21. Levy, D. & Tadmor, E. (1997) *Math. Res. Lett*. **4,** 1–20.
22. Sweby, P. K. (1984) *SIAM J. Numer. Anal.* **21,** 995–1011.
23. Liu, X.-D. & Osher, S. (1996) *SIAM J. Numer. Anal.* **33,** 760–779.
24. Chorin, A. J. (1977) *J. Comp. Physics* **25,** 253–272.